Electronic Supplementary Information

Formation, Aggregation, and Transport of NOM-Cr(III) Colloids in Aquatic Environments

Binrui Li[a], Peng Liao[*,b,c], Peng Liu[a], Dengjun Wang[d], Zhihang Ye[a], Jingfu Wang[b], Jingan Chen[b], Zigong Ning[e], Yi Jiang[f], Chongxuan Liu[*,c]

[a]School of Environment, China University of Geosciences, 388 Lumo Road, Wuhan, 430074, P. R. China

[b]State Key Laboratory of Environmental Geochemistry, Institute of Geochemistry, Chinese Academy of Sciences, Guiyang, 550081, PR China

[c]State Environmental Protection Key Laboratory of Integrated Surface Water-Groundwater Pollution Control, School of Environmental Science and Engineering, Southern University of Science and Technology, Shenzhen, 518055, P. R. China

[d]School of Fisheries, Aquaculture and Aquatic Sciences, Auburn University, Auburn, AL 36849, USA

[e]School of Civil and Environmental Engineering, Harbin Institute of Technology, Shenzhen 518055, China

[f]Department of Civil and Environmental Engineering, The Hong Kong Polytechnic University, Hung Hom, Kowloon, Hong Kong, China

*Corresponding authors:

Peng Liao	Chongxuan Liu
liaopeng@mail.gyig.ac.cn	liucx@sustech.edu.cn

Table of Contents

1. Additional methods and characterization

Section S1: Size fractionation of NOM-Cr(III) samples

Samples collected under equilibrium were analyzed for Cr(III) and NOM concentrations in NOM-Cr(III) samples based on the following size fractionation: truly dissolved species (<10 kDa, roughly equal to <1−3 nm), small colloids (1−3 to 220 nm), large colloids (220−450 nm), and particulates (> 450 nm). These different fractions were separated from samples by 10 kDa ultrafiltration membranes (Amicon Ultra-15, EMD, Millipore), 0.22 μm syringe filters (PES), and 0.45 μm syringe filters (PES). Colloids in this study were defined as particles ranging from 10 kDa to 450 nm. Specifically, the colloidal samples were operationally isolated by the pore size of separating devices; i.e., filtered water samples (filtrates) were separated into permeates (<10 kDa, truly dissolved phase) and retentates (10 kDa −450 nm) by 10 kDa ultrafiltration membranes. Prior to use, all centrifugal ultrafilters were rinsed with DI water multiple times to remove residual glycerol. The truly dissolved fraction of each sample was collected from the filtrates after centrifugal filtration (at 5500 rpm for 20 min). All filtration procedures were conducted at least in triplicate. The colloidal, truly dissolved, and particulate concentrations for each element were determined from the concentrations measured in the unfiltered, 10 kDa ultrafiltration, and 450 nm filtration fractions.

Section S2: Cr K-edge XANES and EXAFS, cryogenic XPS, ATR-FTIR, and Cs-STEM characterizations

Selected suspension samples collected from the end of batch experiments were centrifuged and freeze-dried to yield solids for X-ray absorption fine structure (XAFS), cryogenic X-ray photoelectron spectroscopy (XPS), and attenuated total reflectance Fourier transform infrared (ATR-FTIR) characterizations, respectively. Cr K-edge XANES and EXAFS spectra were collected on samples with molar C/Cr ratios ranging between 0.9 and 21.7 for both AHA-Cr(III) and SRHA-Cr(III) particles at the end of the batch experiments. Samples were freeze-dried and then sandwiched as wet pesters between Kapton film and sealed with Kapton tape. XANES and EXAFS spectra were collected in fluorescence mode on beamline 20-Bending Magnet (20-BM) of the Advanced Photon Source (APS) at Argonne National Laboratory. Spectra of Cr reference compounds including $K_2Cr_2O_7$ and $Cr(OH)_3$ were also collected at the same beamline. Given the relatively low Cr concentrations, all spectra were collected in fluorescence mode in an energy range from −200 to 550 eV relative to 5989 eV, step energy as 5 eV in the pre-edge region, 0.3 eV in XANES region, and 0.05 $Å^{-1}$ in EXAFS region. Three to six scans were performed for each sample. Linear combination fitting (LCF) was performed using Athena[1] in the XANES region from −20 to +30 eV (E_0 as 6004 eV). The raw EXAFS spectra were converted into $k^3\chi(k)$ and Fourier-transformed over k = 2–10 $Å^{-1}$ using the Hanning window function after background removal and normalization. Artemis was used for Cr EXAFS modeling. Structural information derived from the guyanaite (β-CrOOH) was used in EXAFS modeling, and

the structure file of guyanaite was collected from AMCSD.[2] The amplitude reduction factor (S_0^2) was set at 0.805, as obtained from the modeling of $Cr(OH)_3$ spectra. The modeling was conducted over the R range from 1 to 3.4 Å. The coordination number (*CN*), the interatomic distance (*R*), Debye-Waller factor (σ^2), and E_0 difference (ΔE_0) between assigned and theoretical values were set as variables. The goodness of fit was evaluated by the R-factor.

Cryogenic XPS spectra were collected on a PHI 5000 VersaProbe III SXM scanning X ray microprobe equipped with a monochromatic Al Kα source using a pass energy of 58.7 eV. All measurements were performed at cryogenic temperature (−160 °C). The binding energy was calibrated using the adventitious carbon C 1s XPS peak at 284.8 eV as a reference, and the spectra were proceeded using MultiPak v9.8 software. ATR-FTIR spectra were collected using a Thermo Nicolet iS50 FTIR spectrometer equipped with a diamond internal reflection element (IRE). Samples were prepared on the ATR cell by placing the freeze-dried solids evenly onto the diamond crystal surface with a diameter of ~3 mm under an argon environment. A dry cell purged with argon gas was used as a background for all samples. Spectra were collected over the wavelength of 4000 to 500 cm^{-1} at a resolution of 4 cm^{-1}. Data were proceeded using the OMNIC software package.

Suspensions were viewed using ultrahigh-resolution scanning transmission electron microscopy (STEM) to determine the morphology and microstructural composition of NOM-Cr(III) colloids. Samples were prepared by placing a small drop of suspension onto a 10-nm thick window of silicon nitride membrane (SN100, SiMPore Inc, USA).

After drying under ambient conditions, the samples were imaged using a double spherical aberration corrected STEM (Cs-corrected STEM, Thermo Fisher, Themis G2 60-300) using an acceleration voltage of 300 kV and equipped with high angle annular dark field (HAADF) detector and four energy-dispersive X-ray spectroscopy (EDS) detectors.

Section S3: Sampling and characterization of river water and groundwater

The detailed locations of the surface and groundwater sampling points are displayed in Fig. S2. Four groundwater samples and three surface river water samples were collected in the summer of 2019 from a contaminated tidal Maozhou watershed in Pearl River delta, southern China. Three river waters (RW1, RW2, and RW3) were collected from Maozhou River watershed. Four groundwaters (GW1, GW2, GW3, and GW4) were collected from two positions with different depth (2.4−13.5 m). Selective groundwater (GW1) was mixed with the river water (RW1) in different ratios (i.e., groundwater: river water = 1:1, 1:2, 1:2.5, and 1:3) to create an array of solutions representing groundwater-surface water interactions. Groundwater samples were obtained using a small peristaltic pump at a flow rate of 1.0 L/min. Groundwater and surface water samples were filtered within 15−20 min of collection through a 0.22 μm PES membrane, in a precleaned bottle and then carefully filled without headspace. The resulting samples were immediately transported to the laboratory, where it was stored at 4 °C prior to use. Water chemistry characteristics of the water samples were measured within 10 days of sample collection. Conductivity, temperature, pH, and oxygen were

measured by a HQ40D potable meter (HACH, USA). Concentrations of common elements were determined by inductively coupled plasma optical emission spectrometer (ICP-OES) (Optima 8000, Perkin Elmer), inductively coupled plasma mass spectrometer (ICP-MS) (Agilent, 7700 series), and ion chromatograph (ICS-1100, Thermo Scientific). Dissolved organic carbon (DOC) were quantified by a total organic matter (TOC) analyzer (Multi N/C 3100, Analytik Jena, Germany). The characteristics of the water samples are given in Tables S3 and S4.

Section S4: Column experiments

Column experiments were performed to investigate the transport of NOM-Cr(III) colloids and larger particles formed under oxic conditions through sand-packed porous media. Quartz sand with a median diameter of 0.50 mm was chosen as a model porous media. Prior to use, the quartz sand was cleaned using a sequential acid-base deionized water wash procedure.[3,4]

The NOM-Cr(III) influent suspensions were prepared by adding 10 mg/L Cr(III) and different concentrations of AHA to stirred, predetermined volumes (500 mL) of filtered river water (RW3) in the dark, creating molar C/Cr ratios of 1.7 and 21.7. The characteristic of the river water is provided in Table S4. The mixed suspensions were allowed to equilibrate. All suspensions were stored in the dark and they were used within one day of being prepared. During the course of transport experiments, the influent suspensions were continuously stirred on a shaker to maintain suspension stability and avoid any settling of particles.

The column setup is depicted in Fig. S3. A Cylindrical Plexiglas column (2.5 cm i.d. × 10 cm long) was packed with 71.4 g of the cleaned quartz sand, yielding a porosity of 0.47. After packing, the column was pre-equilibrated with 10 pore volumes (PVs) of background solutions (filtered river water) in an upflow mode using a peristaltic pump. The flow rate for all transport experiments was fixed at 1 mL/min, which corresponds to the Darcy velocity of ~2.94 m/day. Following the pre-equilibration, each column received 12 PVs of NOM-Cr(III) suspensions with the same background solution composition, followed by elution with 10 PVs of filtered river water background solution. A nonreactive tracer (200 mg/L KBr) experiment was also performed to determine the hydrodynamic properties of the packed column, including pore-water velocity and dispersivity, which were then used in numerical modeling of the transport of NOM-Cr(III) colloids in the column experiments. The concentration of bromide was measured by an ion selective electrode. Column effluent samples were continuously collected from the outlet every 10 min using an automatic fraction collector (Shanghai HUXI, BSZ-100).

After the completion of each transport experiment, the spatial distribution of NOM-Cr(III) particles retained in the column was determined, using the procedures reported in previous literature[3,4]. Specifically, each column was dismantled and the sand was carefully excavated under gravity and dissected into 10 sections (each roughly 1 cm long) that were each put into 20 mL serum bottles. Ten mL of 1 M HCl solution was added to each bottle, and the bottle was shaken at 150 rpm for 12 h or longer to ensure the complete dissolution of Cr(III) retained in the sand. Cr(III) concentrations in the

effluents and retained in the sand were found to be equal to total Cr concentrations because all Cr were Cr(III) under oxic conditions. Thus, Cr(III) concentrations were determined by ICP-MS. Mass balance was examined by dividing the amounts of Cr(III) in the effluent and retained in the sand with the total amount of Cr(III) injected to the column.

Section S5: Transport model

The attachment-detachment process incorporating Langmuirian dynamics and straining-liberation kinetics considering the depth-dependent retention have been regarded as two major processes to describe the transport and deposition of organic colloids in porous media.[5-10] NOM-Cr(III) colloids formed in this study can be regarded as organic colloids. A one-dimensional form of the advection-dispersion equation (ADE) with two-site kinetic model was thus used to simulate the breakthrough curves (BTCs) and deposition profiles of NOM-Cr(III) colloids. The details of model description were based on our recent work as follows.[9,10]

$$\frac{\partial \theta_w C}{\partial t} + \rho\frac{\partial S_1}{\partial t} + \rho\frac{\partial S_2}{\partial t} = \frac{\partial}{\partial x}\left(\theta_w D\frac{\partial C}{\partial x}\right) - v\frac{\partial C}{\partial x} \quad \text{(S1)}$$

Site 1: Langmuirian attachment

$$\rho\frac{\partial S_1}{\partial t} = \theta_w k_{att}\varphi_{att}C \quad \text{(S2)}$$

$$\varphi_{att} = 1 - \frac{S}{S_{max}} \quad \text{(S3)}$$

Site 2: depth-dependent retention

$$\rho\frac{\partial S_2}{\partial t} = \theta_w k_{str}\varphi_{str}C \quad \text{(S4)}$$

$$\varphi_{str} = (\frac{d+z}{d})^{-\beta} \quad \text{(S5)}$$

where k_{att} is the first-order attachment coefficient rate (T^{-1}), and S_{max} is the maximum solid-phase retention capacity (L^3 M^{-1}) on site 1, k_{str} is the first-order straining coefficient rate (T^{-1}) on site 2, S is the attached colloid concentration (MM^{-1}), C is the aqueous phase colloid concentration (ML^{-3}), θ_w is the volumetric water content (-), ρ is the bulk density (ML^{-3}), v is the pore water velocity (LT^{-1}), D is the dispersion coefficient (-), d is the sand particle diameter (L), z is the distance from column inlet (L), and β is an empirical parameter (β=0.43).[11] The BTCs and deposition profiles were simulated using HYDRUS-1D software (version 4.16.0110). Detailed parameter calculations can be found in our recent work.[8-10]

Section S6: Potential for transport of NOM-Cr(III) colloids in porous media

To evaluate the potential for the transport of NOM-Cr(III) colloids, the maximum transport distance (L_{max}), defined as the distance with 99.9% of the particles retained in the sand, was calculated based on colloid filtration theory.[12,13]

$$L_{max} = -\frac{2}{3(1-\theta)\alpha\eta_0}d\ln(M_{eff}) \quad \text{(S6)}$$

where d is the mean diameter of the collector (sand), θ is the porosity of the packed-column, α is the attachment efficiency (i.e., number of particles that are retained on the sand collector divided by the number of particles that strike the sand collector), η_0 is the theoretical single-collector contact efficiency (i.e., number of particles that strike

the sand collector divided by the number of particles that approach the sand collector), and M_{eff} is the eluent mass recovery of Cr(III) in the transport experiments (see Table S7).

The overall single-collector contact efficiency (η_0) includes the individual contributions of single-collector contact efficiency governed by Brownian diffusion (η_D), interception (η_I), and gravitational sedimentation (η_G), respectively, which can be approximately evaluated using the Tufenkji-Elimelech (T-E) equation.[12]

$$\eta_0 = \eta_D + \eta_I + \eta_G \tag{S7}$$

$$\eta_D = 2.4 A_S^{1/3} N_R^{-0.081} N_{Pe}^{-0.715} N_{vdW}^{0.052} \tag{S8}$$

$$\eta_I = 0.55 A_S N_R^{1.675} N_A^{0.125} \tag{S9}$$

$$\eta_G = 0.22 N_R^{-0.24} N_G^{1.11} N_{vdW}^{0.053} \tag{S10}$$

where A_S is a porosity-dependent parameter, N_R is the aspect ratio, N_{Pe} is the Peclet number (i.e., characterizing the ratio of convective transport to diffusive transport), N_{vdW} is the van der Waals number (i.e., characterizing the ratio of van der Waals interaction energy to the particle's thermal energy), N_A is the attraction number (i.e., characterizing the combined effect of van der Waals attractive force and fluid velocity on particle deposition rate due to interception), and N_G is the gravity number (i.e., characterizing the ratio of Stokes particle settling velocity to approach velocity of the fluid).

Equations for determining A_S, N_R, N_{Pe}, N_{vdW}, N_A, and N_G are given below.

$$A_S = \frac{2(1-\theta^5)}{2-3\theta+3\theta^5-2\theta^6} \tag{S11}$$

$$N_R = \frac{d_p}{d} \tag{S12}$$

where d_p is the diameter of NOM-Cr(III) particle.

$$N_{Pe} = \frac{U d_c}{D_\infty} \tag{S13}$$

where U is the fluid approach velocity; and D_∞ is the bulk diffusion coefficient.

$$N_{vdW} = \frac{A}{kT} \tag{S14}$$

where A is the Hamaker constant of the NOM-Cr(III) colloids, k is the Boltzmann constant, and T is the absolute temperature.

$$N_A = \frac{A}{12\pi\mu a_p^2 U} \tag{S15}$$

where μ is the absolute fluid viscosity of water, and a_p is the particle radius.

$$N_G = \frac{2a_p^2(\rho_p - \rho_f)g}{9 \quad \mu U} \tag{S16}$$

where ρ_p and ρ_f are the densities of particle and fluid, respectively, and g is the gravitational acceleration.

The attachment efficiency (α) can be calculated using the following equation

$$\alpha = -\frac{2 \quad d}{3(1-\theta)L\eta_0} ln_{f0}(M_{eff}) \tag{S17}$$

where L is the length of packed column.

The deposition rate coefficient (k_d) can be given by

$$k_d = \frac{3(1-\theta)}{2 \quad d\theta} U\alpha\eta_0 \tag{S18}$$

Please note that the Hamaker constant and particle density for NOM-Cr(III) colloids and larger particles were not reported previously. Therefore, we are not able to

accurately calculate N_{vdW}, N_A, and N_G, and thus, α and η_0. However, for a given condition, the determination of k_d and L_{max} values were independent of α and η_0, because the overall contribution of Hamaker constant and particle density were counterbalanced in the term of $\alpha\eta_0$ in equations S6, S17, and S18. Consequently, while the Hamaker constant and particle density of NOM-Cr(III) colloids were not determined experimentally, the calculated k_d and L_{max} values were reliable.[13] The T-E equation is a well-defined semiempirical correlation equation and inherently has some assumptions.[12] For example, the T-E equation assumes the spherically-shaped colloids. However, the morphology of NOM-Cr(III) colloids was irregular (see Fig. 4a-d in the main text). Therefore, the T-E equation calculations should be viewed as a rough estimation of k_d and L_{max} of the NOM-Cr(III) colloids in this study. Using the T-E equation, we recently evaluated the k_d and L_{max} of engineered carbon nanotube-magnetite nanohybrids under similar column experimental conditions.[13]

2. Additional results and discussion

Section S7: Investigating NOM complexation with Cr(III) by ATR-FTIR

The complexation of Cr(III) with NOM for NOM-Cr(III) colloid formation was determined by ATR-FTIR. As Fig. S7 shows, the spectra of AHA and SRHA are quite different. The two main peaks in AHA around 1378 and 1567 cm^{-1} were assigned to the symmetric and asymmetric vibrations of the deprotonated form of COO^-, respectively. The spectra of SRHA showed a very strong peak around 1713 cm^{-1} corresponding to

symmetric C=O stretch of undissociated COOH group. The two other main peaks around 1416 and 1614 cm^{-1} were assigned to the asymmetric and symmetric COO^- bands, respectively. After complexation with Cr(III) at pH 7, the spectra of AHA-Cr(III) colloids and SRHA-Cr(III) colloids were distinct from the initial AHA and SRHA. Specifically, the asymmetric and symmetric COO^- bands around 1378 and 1567 cm^{-1} decreased in intensity and shifted to 1355 and 1574 cm^{-1} after AHA complexed with Cr(III). Similarly, the asymmetric and symmetric COO^- bands around 1416 and 1614 cm^{-1} in SRHA sample shifted to a lower wavenumber of 1354 and 1574 cm^{-1} in SRHA-Cr(III) sample. Compared to SRHA, the symmetric C=O band around 1713 cm^{-1} disappeared in SRHA-Cr(III) sample. Since the shift and change in the shape of the stretching bands of COO^- is typically linked to the carboxylate-metal bond formation,[14] the observed shift and change in the band of COO^- is consistent with the proposition that Cr(III) was predominantly complexed with carboxylic groups likely through a ligand exchange mechanism. This agrees well with recent synchrotron-based X-ray spectroscopy results showing that Cr(III) formed stable polynuclear complexes with NOM at neutral pH through carboxyl functional groups.[15]

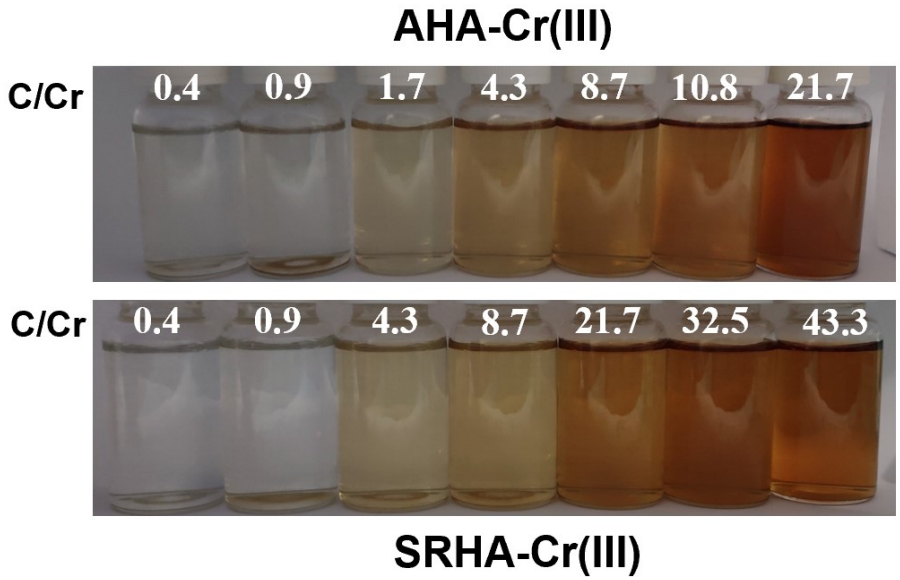

Fig. S1 Photographs of AHA-Cr(III) suspensions (top raw) and SRHA-Cr(III) suspensions (bottom raw) with different initial molar ratios of C/Cr for steady-state conditions. Note that the NOM-Cr(III) suspensions, without any filtration treatments, contained truly soluble, colloidal, and particulate species of Cr(III) and NOM.

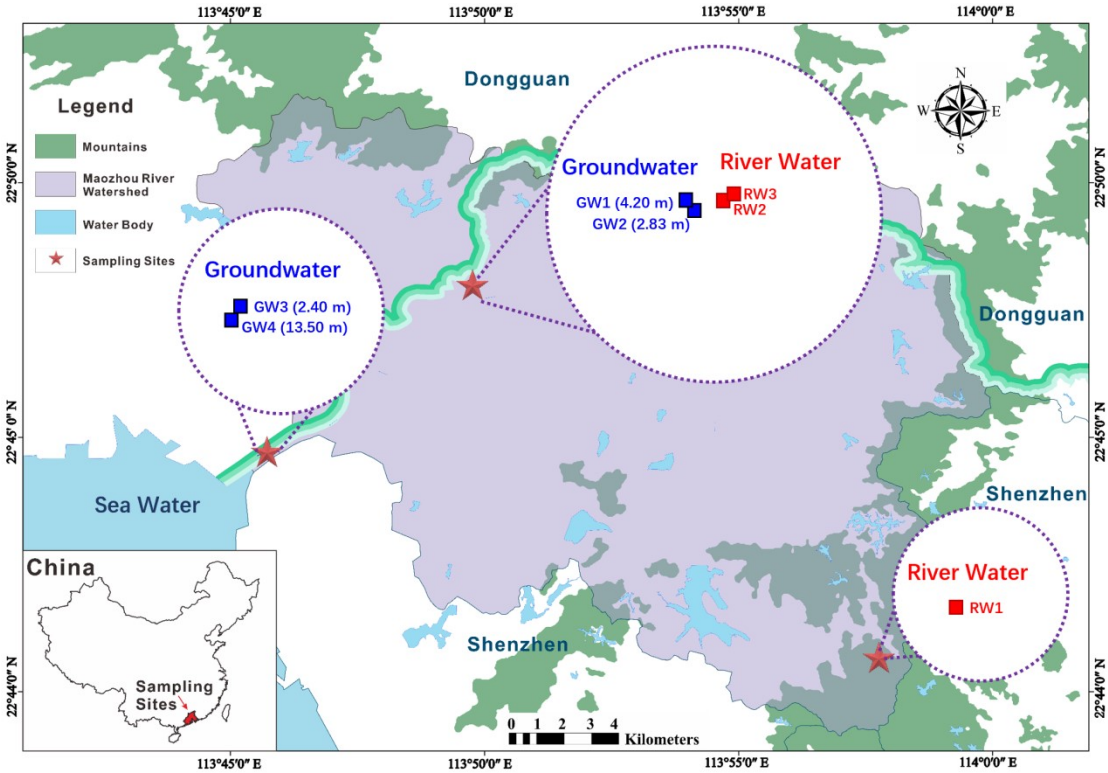

Fig. S2 Locations for river water and groundwater sampling points. Note that the groundwater sampling site was located in groundwater-seawater interaction zone.

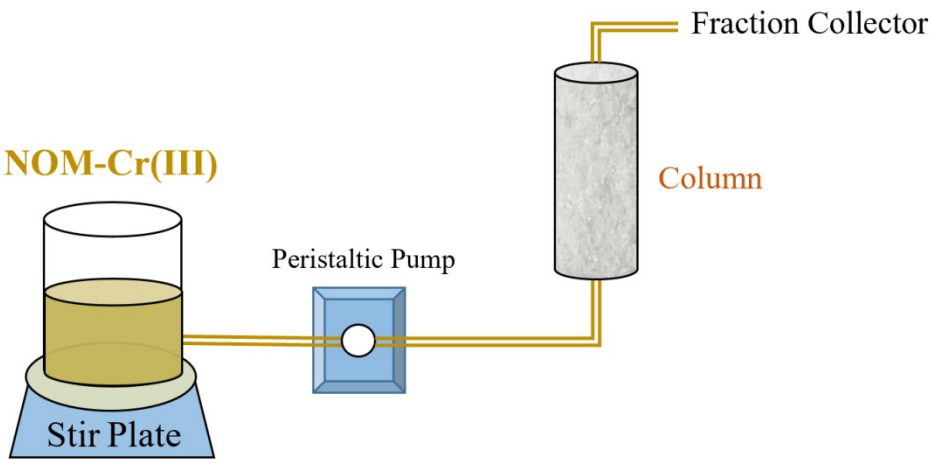

Fig. S3 Schematic of the flow-through reactor system. The principal components were the feed suspension container, peristaltic pump, cylindrical plexiglas columns, and effluent collection system. Influent suspensions were continuously stirring to avoid suspension settlement and maintain suspension stability. All experiments were operated under oxic conditions at room temperature with oxygen saturated conditions and all influent suspensions were covered by aluminum foil to exclude light.

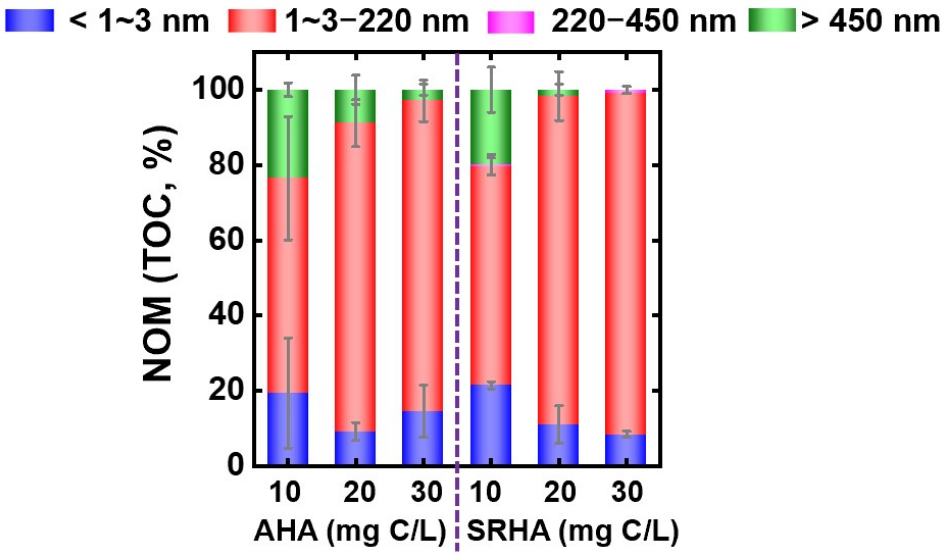

Fig. S4 Percentage of NOM concentrations in AHA and SRHA suspension in the size fractions as a function of initial HA concentrations (control experiments without Cr(III)).

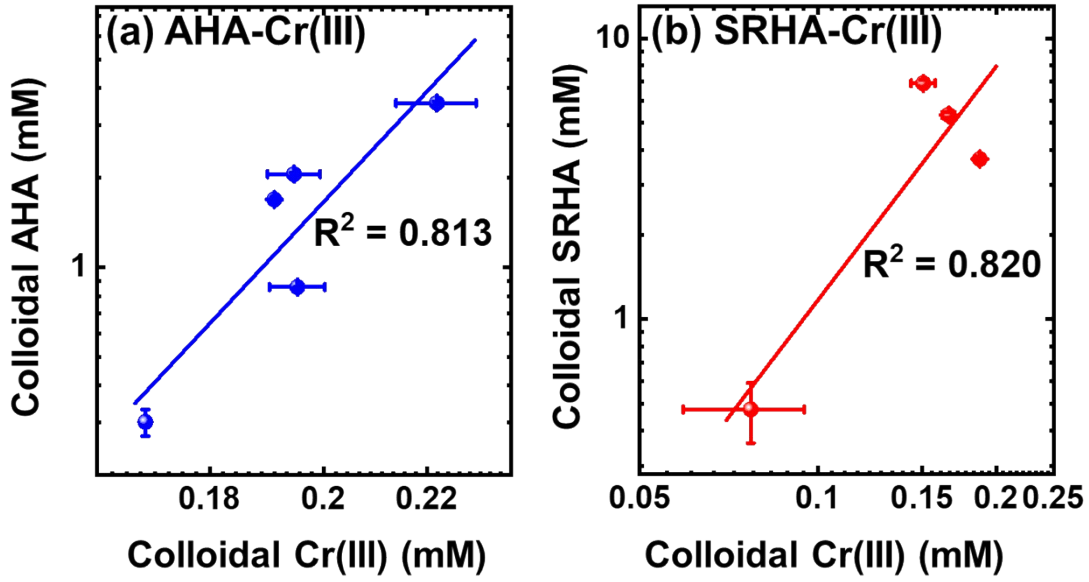

Fig. S5 Correlation between the colloidal Cr(III) concentration and the colloidal (a) AHA and (b) SRHA concentration. Error bars represent standard deviations of at least duplicate measurements.

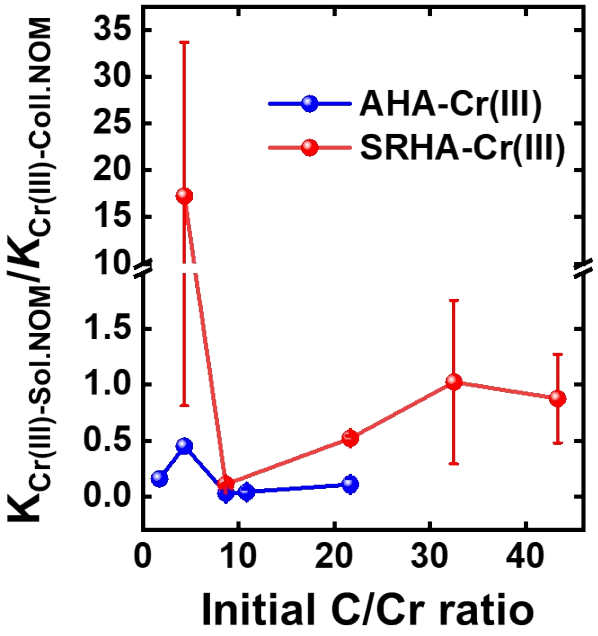

Fig. S6 The evaluated $K_{Cr(III)\text{-}Sol.NOM}/K_{Cr(III)\text{-}Coll.NOM}$ as a function of initial C/Cr molar ratios. $K_{Cr(III)\text{-}Sol.NOM}/K_{Cr(III)\text{-}Coll.NOM}$ = ([Sol. Cr(III)]/[Coll. Cr(III)])×([Coll. NOM]/[Sol. NOM]), where [Sol. Cr(III)] and [Coll. Cr(III)] are the truly soluble and colloidal Cr(III) concentration, respectively, [Sol. NOM] and [Coll. NOM] are the truly soluble and colloidal NOM concentration, respectively.

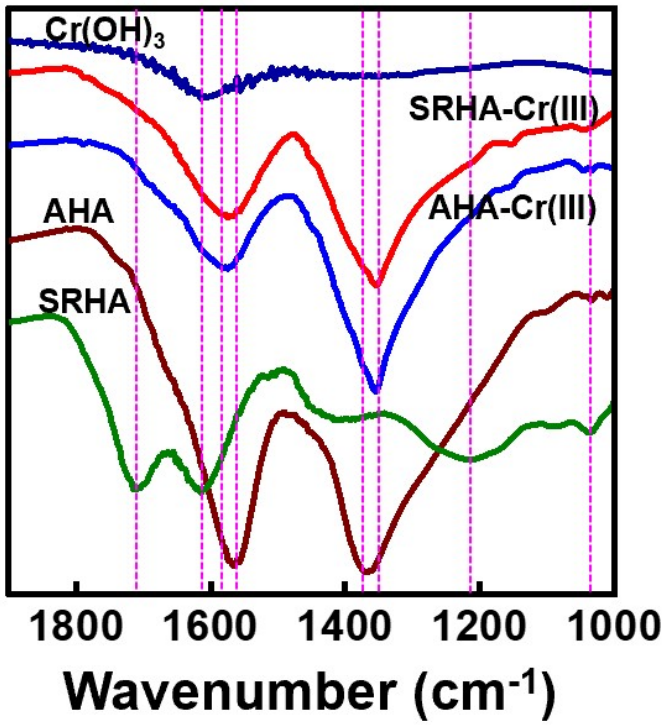

Fig. S7 ATR-FTIR spectra of NOM-Cr(III) colloids collected from the end of the steady-state conditions. ATR-FTIR analysis of NOM-Cr(III) samples were obtained at a fixed initial C/Cr ratio of 21.7. For reference, the patterns of $Cr(OH)_3$, AHA, and SRHA, were included in the ATR-FTIR plots.

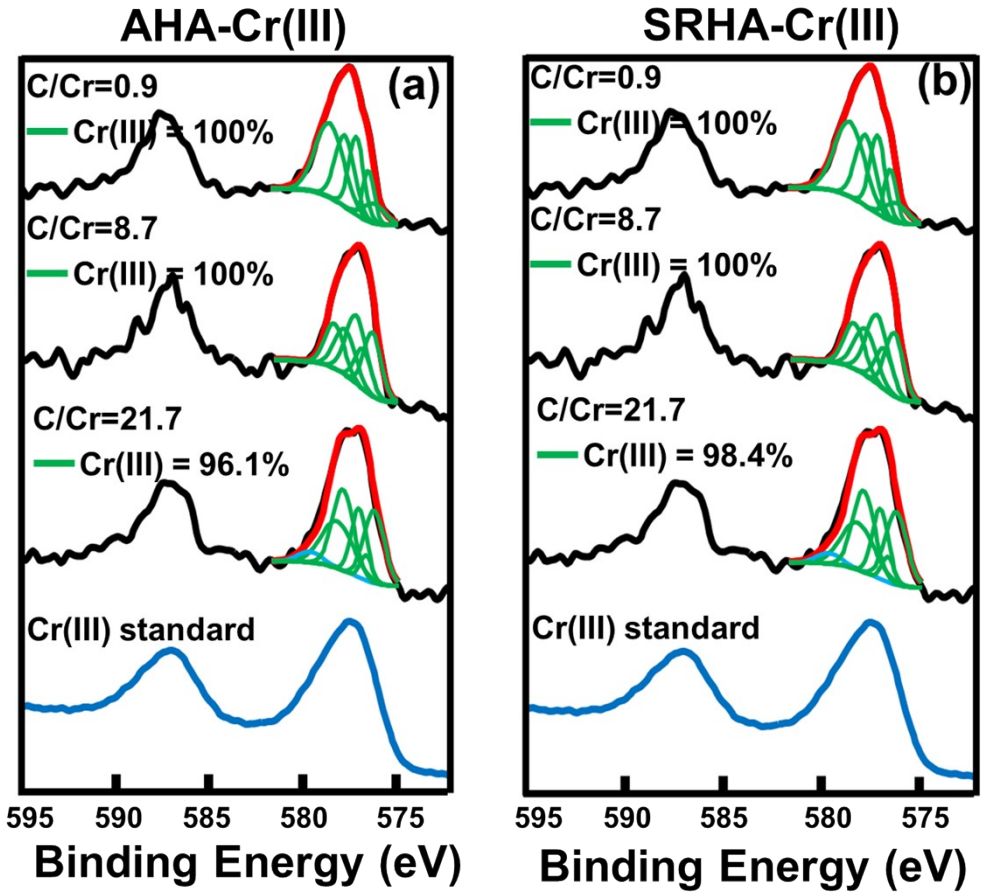

Fig. S8 XPS Cr 2p narrow region spectra and curve-fitting analysis of NOM-Cr solids collected from the end of the steady-state conditions as a function of initial C/Cr molar ratios. All spectra were collected at the surface. Raw data were fitted using a least squares procedure with the Gaussian-Lorentzian function (80% G-20% L) after subtracting a Shirley background. XPS spectra were analyzed by MultiPak v9.8 software. Peak fitting was performed only for the Cr $2p_{3/2}$ peak, due to the complexity of the Cr region. Peak fitting for Cr $2p_{3/2}$ peaks was assigned based on literature-reported values summarized by Biesinger and coworkers.[16-19] For reference, the patterns of $CrCl_3$ was included in the XPS plots.

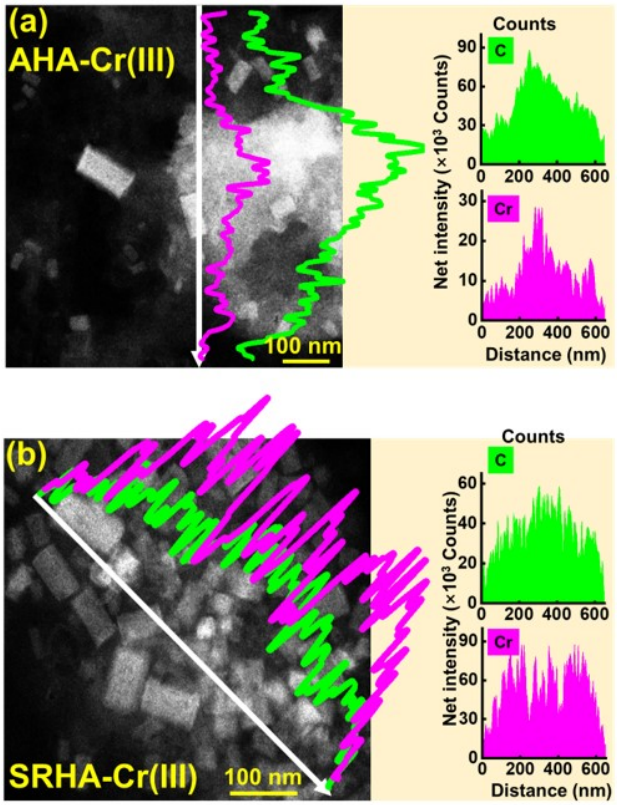

Fig. S9 Representative high-resolution HAADF-STEM-EDS line-scan profiles recorded through the marked line (white) of (a) AHA-Cr(III) colloids and (b) SRHA-Cr(III) colloids under steady-state conditions. Both colloids were imaged at a molar C/Cr ratio of 10.8. HAADF-STEM images and EDS mappings displayed are representative of typical images collected for each sample. All images were taken at a comparable magnification.

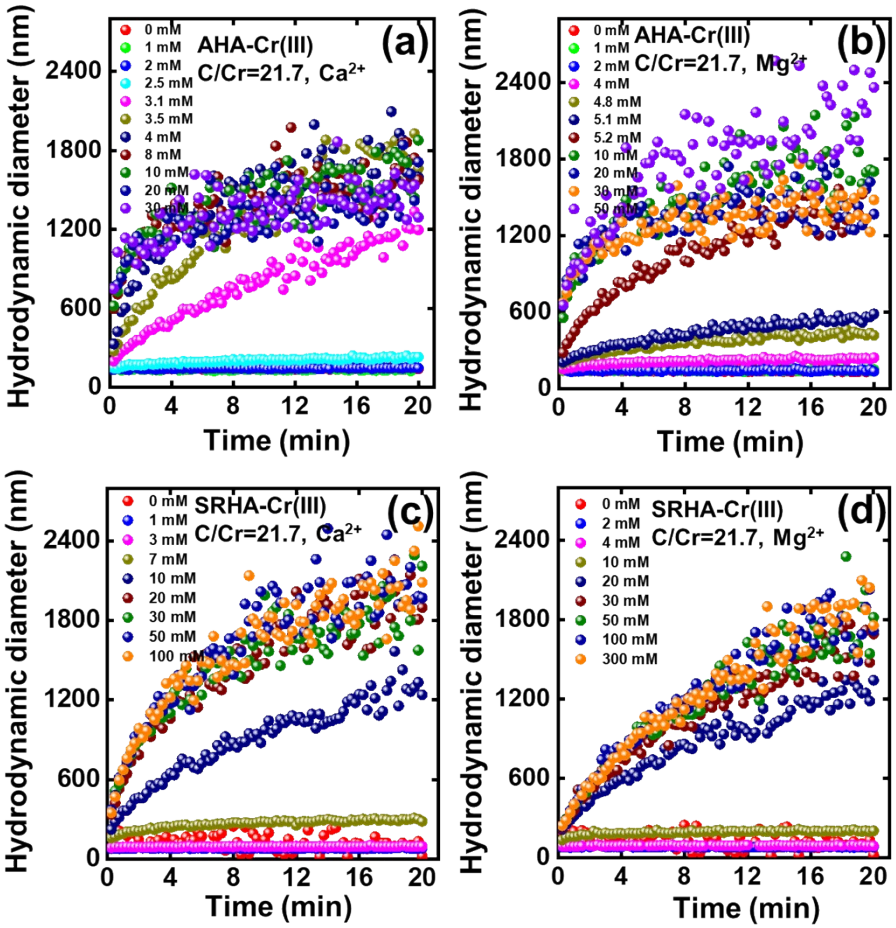

Fig. S10 Representative time-resolved aggregation profile of (a,b) AHA-Cr(III) colloids and (c,d) SRHA-Cr(III) colloids in the presence of different (a,c) Ca^{2+} and (b,d) Mg^{2+}concentrations.

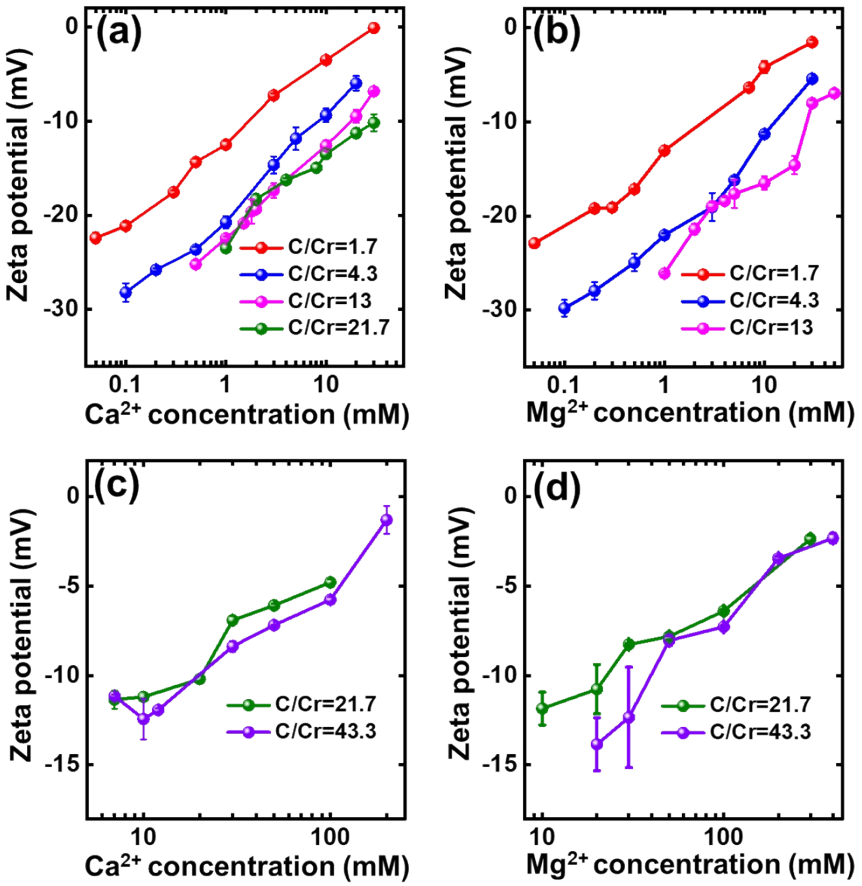

Fig. S11 Zeta potentials of different C/Cr molar ratios of (a,b) AHA-Cr(III) colloids and (c,d) SRHA-Cr(III) colloids respectively over a range of (a,c) Ca^{2+} and (b,d) Mg^{2+} concentrations at pH 7. Each data point shows the mean of 10 measurements of duplicate samples. Error bars represent standard deviations.

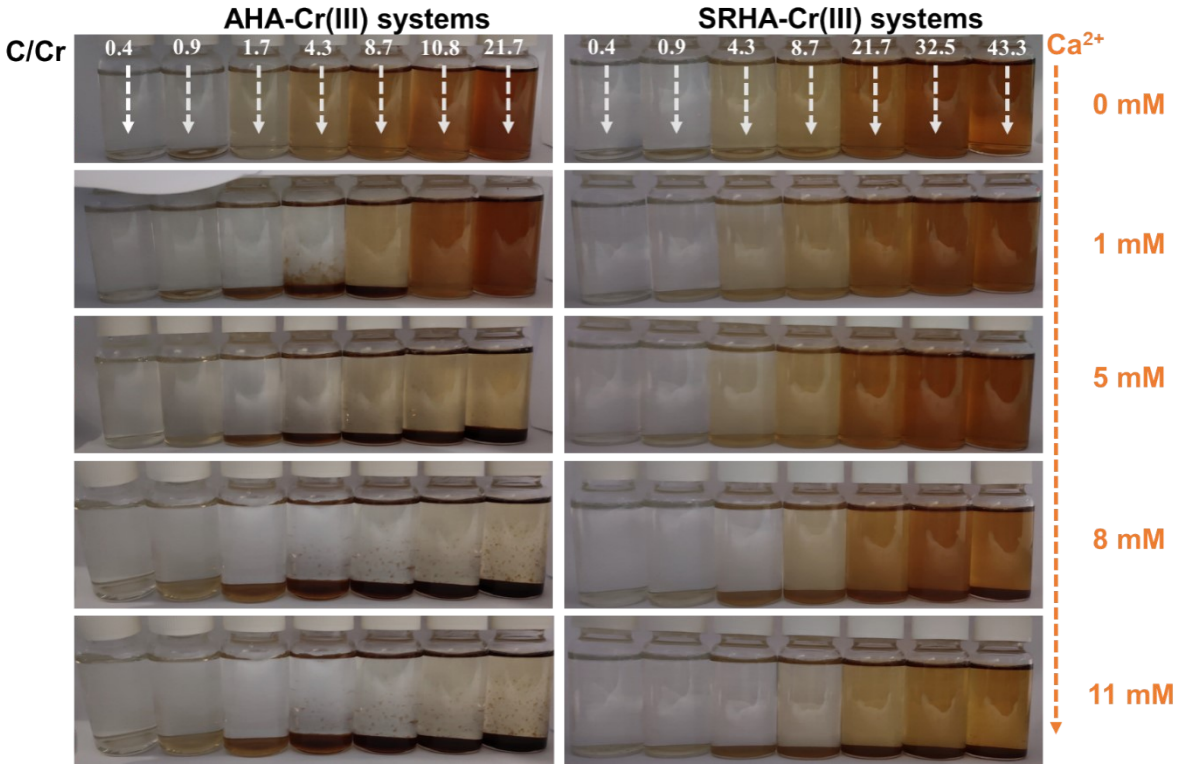

Fig. S12 Photographs of AHA-Cr(III) suspensions (left) and SRHA-Cr(III) suspensions (right) with different molar ratios of C/Cr in the presence of different Ca^{2+} concentrations for steady-state conditions.

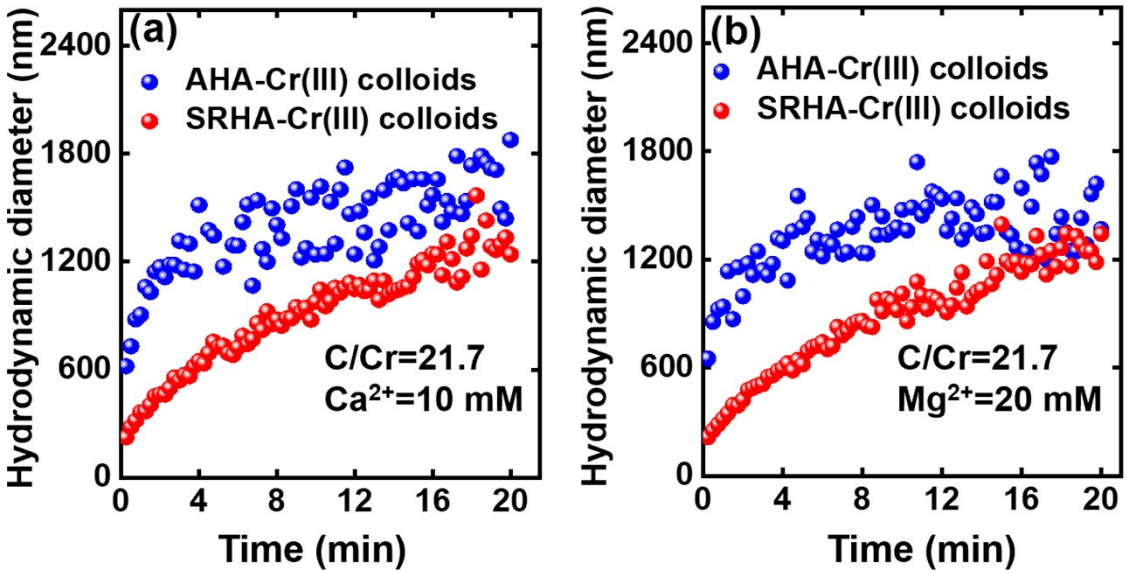

Fig. S13 Representative comparison of size evaluation of AHA-Cr(III) colloids and SRHA-Cr(III) colloids formed at a molar C/Cr ratio of 21.7 in the presence of (a) Ca^{2+} and (b) Mg^{2+}.

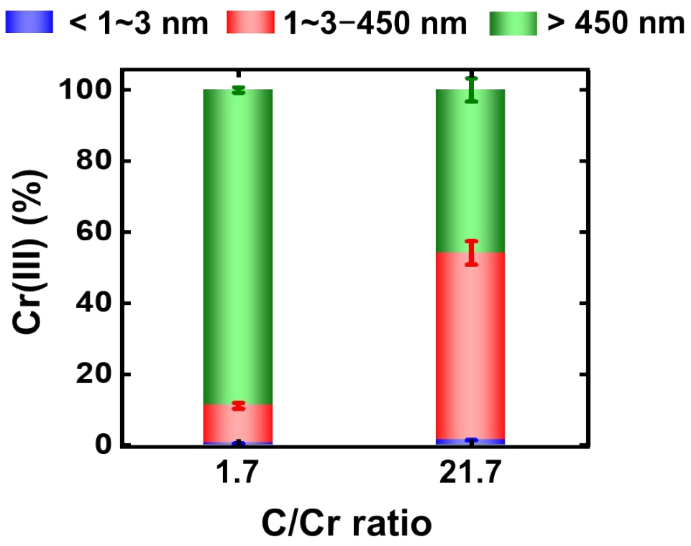

Fig. S14 Percentage of Cr(III) concentration in AHA-Cr(III) influent suspension prepared in river water (RW3) under steady-state conditions as a function of initial C/Cr molar ratios. The percentage in y-axis means the concentration of Cr(III) in a certain size fraction to the total concentration of Cr(III) in the suspension.

Table S1 Characteristics of NOM isolates used in this study

Sample	Bulk elemental composition[a] (%)					Functional group composition[b]				$SUVA_{254}$ [c]	Hydrodynamic diameter[d]
	C	H	O	N	S	Carbonyl	Carboxyl	Aromatic	Aliphatic	L/(mg·m)	(nm)
AHA	47.3	3.1	44.9	1.2	3.5	14	15.6±2.2	40	41	9.5 ± 0.4	181±47
SRHA	54.59	3.9	40.03	1.5	0.55	3.9	12.8	35.3	23.9	6.3 ± 0.3	135±59

[a]Bulk elemental compositions and [b]Functional group composition for SRHA were provided by International Humic Substances society (IHSS, http://humic-substances.org/). [a]Bulk elemental compositions for AHA were determined by Vario Micro cube elemental analyzer as previously reported.[20] [b]Functional group composition for AHA were determined by ^{13}C nuclear magnetic resonance (NMR) as reported.[21,22] [c]Specific UV absorbance ($SUVA_{254}$) for both NOM were determined by diluting NOM stock solutions to different concentrations (i.e., 1−10 mg C/L) and measure their UV absorbance at 254 nm using a UV-vis spectrophotometer (Cary 60, Agilent).[23] [d]Hydrodynamic diameter was measured by dynamic light scattering (DLS) (Marvern) at pH 7.

Table S2 Summary of the batch experiments for colloid formation and stability[a]

expt[b]	NOM source	Initial NOM mg C/L	Initial Cr(III) mg/L	Initial C/Cr mole ratio	pH
1		0	10	0	7
2	AHA	1	10	0.4	7
3	AHA	2	10	0.9	7
4	AHA	4	10	1.7	7
5	AHA	10	10	4.3	7
6	AHA	20	10	8.7	7
7	AHA	25	10	10.8	7
8	AHA	50	10	21.7	7
9	AHA	10	0	−	7
10	AHA	20	0	−	7
11	AHA	30	0	−	7
12	SRHA	1	10	0.4	7
13	SRHA	2	10	0.9	7
14	SRHA	10	10	4.3	7
15	SRHA	20	10	8.7	7
16	SRHA	50	10	21.7	7
17	SRHA	75	10	32.5	7
18	SRHA	100	10	43.3	7
19	SRHA	10	0	−	7
20	SRHA	20	0	−	7
21	SRHA	30	0	−	7

[a]All experiments were conducted under oxic conditions. [b]Results of batch experiments 1−21 were averages of at least duplicate experiments. The ionic strength contributed by NaOH/HCl (controlled pH 7) was <1 mM.

Table S3 Characteristics of groundwater and river water used for NOM-Cr(III) colloid stability experiments [a]

constituent	unit	GW1	GW2	GW3	GW4	RW1	RW2
Ca^{2+}	mg/L	292.6	123.5	355.6	273.6	2.4	34.9
Mg^{2+}	mg/L	205.8	18.6	125.6	178.4	0.6	3.6
F^-	mg/L	ND	ND	ND	ND	0.05	0.33
Cl^-	mg/L	8223.8	82.3	1747.1	4467.8	3.3	46.8
NO_3^-	mg/L	ND	ND	ND	ND	2.0	13.7
SO_4^{2-}	mg/L	970.8	211.8	351.9	417.1	1.5	70.0
total Cd	µg/L	ND	ND	ND	ND	ND	ND
total Mn	µg/L	907.6	804.6	3260.0	2552.8	5.7	211.9
total Fe	µg/L	1031.0	1794.2	1440.3	433.7	31.3	130.7
total Co	µg/L	0.06	0.8	0.3	0.2	ND	0.7
total Ni	µg/L	0.3	2.8	7.1	0.7	0.3	22.2
total Cu	µg/L	ND	2.7	1.9	0.1	0.4	4.0
total Zn	µg/L	ND	69.7	8.8	ND	6.4	12.8
total As	µg/L	ND	1.7	1.2	0.8	ND	1.4
total Pb	µg/L	ND	ND	ND	ND	ND	ND
DOC	mg/L	4.4	6.6	37.4	50.0	4.0	6.4
EC	µS/cm	24700	1213	6920	14340	103.4	512
pH	_	6.84	6.67	6.99	6.99	7.35	7.12

[a]ND=Not detected.

Table S4 Characteristics of the river water used for column experiments

constituent	unit	RW3
Ca^{2+}	mg/L	21.9
Mg^{2+}	mg/L	3.5
F^-	mg/L	0.44
Cl^-	mg/L	84.9
NO_3^-	mg/L	30.6
SO_4^{2-}	mg/L	87.0
total Al	µg/L	5.9
total Mn	µg/L	95.1
total Fe	µg/L	12.4
total Co	µg/L	0.8
total Ni	µg/L	22.2
total Cu	µg/L	3.2
total Zn	µg/L	4.3
total As	µg/L	1.4
total Pb	µg/L	0.05
DOC	mg/L	23.7
EC	µS/cm	722

Table S5 Selected physicochemical properties of NOM-Cr(III) colloids at various conditions

NOM source	bulk C/Cr	XPS probing depth[a] (nm)	surface elemental composition[b] (%)			Surface[c] C/Cr	Colloid[d] C/Cr
			C	O	Cr		
AHA	0.9	0	59.1	38.8	2.1	122.0	–
		10	47.7	45.4	6.8	30.4	
		30	47	43.7	9.4	21.7	
		50	49.2	40.7	10	21.3	
	8.7	0	59.7	37.7	2.6	99.5	8.6
		10	57.1	36.7	6.3	39.3	
		30	52.3	38.6	9	25.2	
		50	49.2	41.3	9.5	22.4	
	21.7	0	48.6	49.6	1.8	117.0	18.5
		10	50.1	45.1	4.8	45.2	
		30	52.5	40.8	6.7	34.0	
		50	52.2	40.9	6.9	32.8	
SRHA	0.9	0	61.3	37.2	1.5	177.1	–
		10	57.1	36.7	6.3	39.3	
		30	57.9	14.5	27.6	9.1	
		50	58.1	10.4	31.6	8.0	
	8.7	0	63.8	34.8	1.3	212.7	7.7
		10	45.8	45.3	8.9	22.3	
		30	49.8	38.5	11.7	18.4	
		50	52.9	35.3	11.8	19.4	
	21.7	0	56	41.9	2	121.3	20.1
		10	43.9	50.3	5.8	32.8	
		30	35.1	56.2	8.7	17.5	
		50	31.6	58.4	10	13.7	

[a]Four XPS probing depths were analyzed. [b,c]Surface elemental composition and surface C/Cr ratio were analyzed by XPS. [d]Determined based on the concentrations of Cr and NOM in colloidal fractions as shown in Fig. 1 in the main manuscript.

Table S6 Parameters of the Cr K-edge XANES LCF and EXAFS modeling results[a]

Sample	LCF		EXAFS modeling					
	$Cr(OH)_3$	R-factor	path	*CN*	σ^2(Å^2)	*R*(Å)	ΔE_0(eV)	R-factor
AHA-Cr	100%	0.0004	Cr-O	6.0(0.8)	0.002	1.98(0.01)	-2.4	0.015
C/Cr=0.9			Cr-Cr	2.1(0.4)	0.006[b]	3.03(0.02)		
AHA-Cr	100%	0.0012	Cr-O	5.5(1.1)	0.001	1.98(0.01)	-1.3	0.035
C/Cr=21.7			Cr-Cr	1.1(0.7)	0.006[b]	3.00(0.04)		
SRHA-Cr	100%	0.0006	Cr-O	6.0(0.9)	0.002	1.98(0.01)	-1.1	0.019
C/Cr=0.9			Cr-Cr	2.4(0.5)	0.006[b]	3.04(0.02)		
SRHA-Cr	100%	0.0008	Cr-O	5.7(1.0)	0.002	1.97(0.01)	-3.2	0.026
C/Cr=21.7			Cr-Cr	1.6(0.6)	0.006[b]	2.97(0.03)		

[a]R-factor is the goodness of fitting or modeling parameters; *CN* is the coordination number; *R* is the interatomic distance; σ^2 is Debye-Waller factor (a disorder parameter); ΔE_0 is the energy difference in the threshold Fermi level between the data and theory. [b]Constrained value in the modeling.

Table S7 Summary of column experiments for mass balance percentages of Cr(III)

Column	Initial conditions (mg/L)			Mass balance (%)			
No	AHA	Cr(III)	molar C/Cr	M_{eff}[a]	M_{ret}[b]	$M_{ret\text{-}inlet}$[c]	M_{total}[d]
1	4	10	1.73	2.7±0.2	50.0±4.6	93.5±2.4	52.4±4.1
2	50	10	21.67	85.4±1.1	6.0±0.1	26.9±4.2	91.4±1.3

[a]M_{eff} refers to the percentage of Cr(III) passing through the column. M_{ret} refers to the percentage of Cr(III) retained in the column. $M_{ret\text{-}inlet}$ is the percentage of retained Cr(III) that are deposited near the column inlet (0–3 cm). M_{tot} denotes the total percentage of Cr(III) recovered from the column ($M_{tot}=M_{eff}+M_{ret}$). Mass balance was calculated by dividing the amounts of Cr(III) in the effluent and retained in the sand with the total amount of Cr(III) (from NOM-Cr(III) suspension) injected into the column. The observation of a low mass recovery (M_{tot} = 52.4±4.1%) for low C/Cr ratio suggests that most Cr(III) precipitated in the influent fitting or tubing as solid phases that were not pumped into the column.

Table S8 Fitting parameters for two-site kinetic model

Expt	Initial C/Cr molar ratio	k_{str}[a] (min^{-1})	k_{att}[b] (min^{-1})	S_{max}[c] ($cm^3\ g^{-1}$)	R^2
1	C/Cr=1.7	2.331±0.212	0.053±0.007	0.016±0.007	0.370
2	C/Cr=21.7	0.046±0.001	0.048±0.001	0.011±0.001	0.801

[a]k_{str} refers to the first-order straining coefficient rate (T^{-1}), [b]k_{att} is the first-order attachment coefficient rate (T^{-1}), [c]S_{max} is the maximum solid-phase retention capacity ($L^3\ M^{-1}$).

References

1 B. Ravel and M. Newville, ATHENA, ARTEMIS, HEPHAESTUS: data analysis for X-ray absorption spectroscopy using IFEFFIT, *J. Synchrotron Radiat.,* 2005, **12**, 537–541.

2 R. T. Downs and M. Hall-Wallace, The American Mineralogist Crystal Structure Database, *Am. Mineral.,* 2003, **88**, 247–250.

3 P. Liao, S. H. Yuan and D. J. Wang, Impact of redox reactions on colloid transport in saturated porous media: An example of ferrihydrite colloids transport in the presence of sulfide, *Environ. Sci. Technol.,* 2016, **50**, 10968–10977.

4 P. Liao, W. L. Li, D. G. Wang, Y. Jiang, C. Pan, J. D. Fortner and S. H. Yuan, Effect of reduced humic acid on the transport of ferrihydrite nanoparticles under anoxic conditions, *Water Res.* 2017, **109**, 347–357.

5 G. Gargiulo, S. Bradford, J. Simunek, P. Ustohal, H. Vereecken and E. Klumpp, Bacteria transport and deposition under unsaturated conditions: the role of the matrix grain size and the bacteria surface protein, *J. Contam. Hydrol*., 2007, **92**, 255–273.

6 S. A. Bradford, Y. S. Wang, H. Kim, S. Torkzaban and J. Simunek, Modeling microorganism transport and survival in the subsurface, *J. Environ. Qual*., 2014, **43**, 421–440.

7 H. Bai, N. Cochet, A. Pauss and E. Lamy, Bacteria cell properties and grain size impact on bacteria transport and deposition in porous media, *Colloids Surf. B,* 2016, **139**, 148–155.

8 D. J. Wang, Y. Jin, C. M. Park, J. Y. Heo, X. Bai, N. Aich and C. M. Su, Modeling the transport of the "New-Horizon" reduced graphene oxide-metal oxide nanohybrids in water-saturated porous media, *Environ. Sci. Technol.*, 2018, **52**, 4610–4622.

9 Z. G. Ning, R. Li, K. T. Lian, P. Liao, H. H. Liao and C. X. Liu, Transport and retention of Shewanella oneidensis strain MR1 in water-saturated porous media with different grain-surface properties, *Chemosphere*, 2019, **233**, 57–66.

10 Z. G. Ning, R. Li, H. S. Lian, S. Zhou, P. Liao and C. X. Liu, Effects of flow-interruption on the bacteria transport behavior in porous media, *J. Hydrol*., 2021, **595**, 125677.

11 S. A. Bradford, J. Simunek, M. Bettahar, M. T. Van Genuchten and S. R. Yates, Modeling colloid attachment, straining, and exclusion in saturated porous media, *Environ. Sci. Technol.*, 2003, **37**, 2242–2250.

12 N. Tufenkji and M. Elimelech, Correlation equation for predicting single-collector efficiency in physicochemical filtration in saturated porous media, *Environ. Sci. Technol.,* 2004, **38**, 529–536.

13 D. J. Wang, C. M. Park, A. Masud, N. Aich, and S. M. Su, Carboxymethylcellulose mediates the transport of carbon nanotube-magnetite nanohybrid aggregates in water-saturated porous media, *Environ. Sci. Technol*., 2017, **51**, 12405–12415.

14 P. Sharma, J. Ofner and A. Kappler, Formation of binary and ternary colloids and dissolved complexes of organic matter, Fe and As, *Environ. Sci. Technol.,* 2010, **44**, 4479–4485.

15 J. P. Gustafsson, I. Persson, A. G. Oromieh, J. W. J. van Schaik, C. Sjostedt and D. B. Kleja, Chromium(III) complexation to natural organic matter: mechanisms and modeling, *Environ. Sci. Technol*., 2014, **48**, 1753–1761.

16 M. C. Biesinger, C. Brown, J. R. Mycroft, R. D. Davidson and N. S. McIntyre, X-ray photoelectron spectroscopy studies of chromium compounds, *Surf. Interface Anal., 2004,* **36**, 1550–1563.

17 M. C. Biesinger, Pa Resolving surface chemical states in XPS analysis of first row transition metals, oxides and hydroxides: Cr, Mn, Fe, Co and Ni, *Appl. Surf. Sci.*, 2011, **257**, 2717–2730.

18 A. P. Grosvenor, B. A. Kobe, M. C. Biesinger and N. S. McIntyre, Investigation of multiplet splitting of Fe 2p XPS spectra and bonding in iron compounds, *Surf. Interface Anal.*, 2004, **36**, 1564–1574.

19 S. A. Saslow, W. Um, C. I. Pearce, M. H. Engelhard, M. E. Bowden, W. Lukens, I. I. Leavy, B. J. Riley, D. S. Kim, M. J. Schweiger and A. K. Kruger, Reduction and simultaneous removal of ^{99}Tc and Cr by $Fe(OH)_2$(s) mineral transformation, *Environ. Sci. Technol.,* 2017, **51**, 8635–8642.

20 Q. Q. Li, L. Xie, Y. Jiang, J. D. Fortner, K. Yu, P. Liao and C. X. Liu, Formation and stability of NOM-Mn(III) colloids in aquatic environments, *Water Res.,* 2019, **149**, 190−201.

21 Y. Jiang, R. Raliva, P. Liao, P. Biswasa and J. D. Fortner, Graphene oxides in water: assessing stability as a function of material and natural organic matter properties, *Environ. Sci. Nano,* 2017, **4**, 1484–1493.

22 J. D. Mao, W. G. Hu, K. Schmidt-Rohr, G. Davies, E. A. Ghabbour and B. S. Xing, Quantitative characterization of humic substances by solid-state carbon-13 nuclear magnetic resonance, *Soil Sci. Soc. Am. J.*, 2000, **64**, 873−884.

23 P. Liao, Y. Z. Liang and Z. Q. Shi, Impact of divalent cations on dark production of hydroxyl radicals from oxygenation of reduced humic acids at anoxic−oxic interfaces, *ACS Earth Space Chem*., 2019, **3**, 484−494.